Materials Science and Engineering B 198 (2015) 10–13

Contents lists available at ScienceDirect

Materials Science and Engineering B

journal homepage: www.elsevier.com/locate/mseb

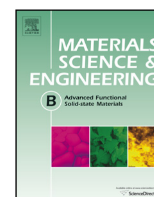

Surface passivation and conversion of SnO_2 to SnS_2 nanowires

M. Zervos [a,*], C.N. Mihailescu [b,d], J. Giapintzakis [b], A. Othonos [c], C.R. Luculescu [d]

[a] Nanostructured Materials and Devices Laboratory and Department of Mechanical and Manufacturing Engineering, University of Cyprus, P.O. Box 20537, Nicosia 1678, Cyprus
[b] Nanotechnology Research Center and Department of Mechanical and Manufacturing Engineering, University of Cyprus, P.O. Box 20537, Nicosia 1678, Cyprus
[c] Center of Ultrafast Science, Nanotechnology Research Center and Department of Physics, University of Cyprus, P.O. Box 20537, Nicosia 1678, Cyprus
[d] National Institute for Laser, Plasma and Radiation Physics, Str. Atomistilor, P.O. Box MG-36, 077125 Magurele, Romania

ARTICLE INFO

Article history:
Received 22 October 2014
Received in revised form 4 March 2015
Accepted 17 March 2015
Available online 28 March 2015

Keywords:
Tin oxide
Tin disulphide
Nanowires
Sulphur passivation

ABSTRACT

SnO_2 nanowires have been grown on Si(0 0 1) via the vapour–liquid–solid mechanism at 800 °C and then exposed to H_2S between 300 and 600 °C. The SnS_2/SnO_2 nanowires obtained at 300 °C consist of tetragonal rutile SnO_2 and hexagonal SnS_2, exhibited defect related photoluminescence at 2.4 eV and have smaller resistances than the SnO_2 nanowires. We show how the Fermi level pinning at the surface of a SnS_2/SnO_2 nanowire would lead to an increase of the one dimensional electron gas density, smaller barrier height and resistance. The SnO_2 nanowires are fully converted into hexagonal SnS_2 at 400 °C resulting into photoluminescence at 2.4 and 2.8 eV but have considerably larger resistances than the SnO_2 nanowires which are eliminated and converted into SnS_2 crystals above 400 °C.

© 2015 Elsevier B.V. All rights reserved.

1. Introduction

Semiconductor nanowires (NWs) have been investigated as emerging devices in view of the ongoing downscaling of integrated circuits but also in the context of nanotechnology for energy conversion and the fabrication of NW solar cells (NWSCs) [1]. One of the main issues related to NWSCs is the suppression of surface recombination due to the large surface to volume ratio. Sulphur passivation of III–V NWs such as InAs and GaAs NWs has been shown to improve their electrical and optical properties [2–6] but this has not been applied to metal oxide (MO) NWs despite the fact that sulphur passivation has been used to isolate the surface from the bulk of ZnO [7] and as a result increase its photoluminescence [8]. The surface passivation of MO NWs is also necessary in order to suppress the adsorption and desorption of oxygen and consequently charge fluctuations and this has been achieved by applying polyimide and polymethylmethacrylate on ZnO and SnO_2 NWs, respectively [9,10]. However, there are no investigations on the surface passivation of MO NWs using H_2S which may also lead to the formation of metal sulphide (MS) NWs such as SnS_2. Tin disulphide has been used for the fabrication of solar cells [11], sensors [12], while it has been shown that SnO_2/SnS_2 core–shell nanoparticles (NPs) have better photocatalytic performance compared to their constituents [13]. SnS_2 has a hexagonal cadmium iodide (CdI_2) structure which consists of layers of Sn atoms surrounded by close packed layers of S atoms with lattice constants of $a = b = 0.365$ nm, $c = 0.589$ nm so it is similar to MoS_2 which has recently attracted attention for the fabrication of nanoelectronic devices such as field effect transistors as an alternative to graphene [14,15] and has also been used for the fabrication of super capacitors and batteries. Tin disulphide has been grown mainly by hydrothermal and solvothermal methods. More specifically, SnS_2 polycrystalline layers have been obtained via the reaction of $SnCl_2$ and $Na_2S_2O_3$ [16], SnS_2 nanobelts from $SnCl_2{\cdot}H_2O$ and Na_2S using thioglycollic acid while SnS_2 NWs have been obtained via the sulphurization of templated Sn NWs in Al_2O_3 [17]. Despite these efforts very little is known about the physical properties of SnS_2 NWs.

Hence we have carried out an investigation into the effect of sulphur passivation on the structural, electrical and optical properties of SnO_2 and the conversion of SnO_2 into SnS_2 NWs using H_2S between 300 and 600 °C for 60 min. We observe the existence of the tetragonal rutile crystal structure of SnO_2 and hexagonal SnS_2 after the exposure of SnO_2 NWs to H_2S at 300 °C for 30 and 60 min, as confirmed by energy dispersive X-ray (EDX) analysis and grazing incidence X-ray diffraction (GIXD). These SnO_2/SnS_2 NWs exhibited defect-related photoluminescence at 2.4 eV and had smaller resistances compared to SnO_2 NWs which is attributed to a change of the Fermi level pinning at the surface of SnS_2 resulting in a smaller barrier height, smaller depletion and higher carrier density. However the conversion of SnO_2 into hexagonal SnS_2 NWs at

* Corresponding author. Tel.: +357 22894509.
E-mail address: zervos@ucy.ac.cy (M. Zervos).

http://dx.doi.org/10.1016/j.mseb.2015.03.006
0921-5107/© 2015 Elsevier B.V. All rights reserved.

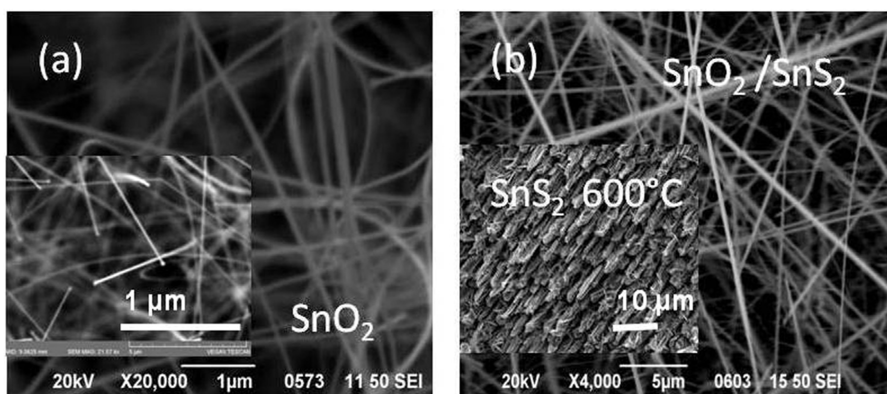

Fig. 1. (a) SnO_2 NWs on Si(0 0 1); inset shows nanoparticle at the top of the SnO_2 NWs, (b) SnS_2/SnO_2 NWs obtained from SnO_2 NWs exposed to H_2S at 300 °C for 60 min; inset shows the elimination of the SnO_2 NWs under H_2S at 600 °C.

400 °C resulted in the appearance of an additional photoluminescence peak at 2.8 eV and considerably higher resistances than the SnO_2 NWs.

2. Methods

SnO_2 NWs were grown using a low-pressure chemical vapour deposition (LPCVD) reactor. For the growth of SnO_2 NWs, Sn (Aldrich, 2–14 mesh, 99.9%) was weighed with an accuracy of ±1 mg. Square samples of Si(0 0 1) ≈7 mm × 7 mm were cleaned sequentially in trichloroethylene, methanol, acetone, isopropanol, rinsed with de-ionised water, dried with nitrogen and coated with ≈1–5 nm Au by sputtering. Following this 0.2 g Sn and the 1 nm Au/Si(0 0 1) substrates were loaded inside the 1″ quartz tube (QT) that was pumped down to 10^{-4} mbar and subsequently purged with 600 sccms of Ar for 10 min at 1 mbar after which the temperature was ramped up to 800 °C using a ramp rate of 30 °C/min while maintaining the same flow of Ar. Upon reaching 800 °C, a small flow of 10 sccms O_2 was added to the main flow of Ar in order to grow the SnO_2 NWs over 60 min after which the reactor was allowed to cool down without O_2. The morphology of the SnO_2 NWs was determined by scanning electron microscopy (SEM) while their crystal structure was determined by GIXD using a Rigaku Smart Lab diffractometer (9 kW rotating Cu-anode) with Cu-$K_{\alpha 1}$ radiation. Subsequently the SnO_2 NWs were exposed to 20 sccm Ar:50 sccm H_2S between 300 and 600 °C for 60 min using a ramp rate of 10 °C/min. In addition SnO_2 NWs were exposed to H_2S at 300 °C and 400 °C for 30 min using the same gas flow of 20 sccm Ar:50 sccm H_2S. All of the SnO_2 NWs were inspected by SEM after exposure to H_2S in order to determine changes in morphology while their crystal structure and phase purity was determined again by GIXD. The composition was determined by EDX using a FEI SEM Inspect S equipped with a Si(Li) detector from EDAX Inc. In addition photoluminescence (PL) was measured with UV excitation of λ = 266 nm at 300 K. Finally SnO_2 NWs were grown on 10 mm × 10 mm fused silica substrates under the same growth conditions and then exposed to H_2S at 300 °C and 400 °C. Their resistances were measured between silver paste contacts deposited at the four corners of the SnO_2 and SnS_2/SnO_2 NW assemblies on the 10 mm × 10 mm fused silica similar to O'Dwyer et al. [18] in order to obtain an estimate of the resistance of the assembly before and after exposure to H_2S.

3. Results and discussion

The reaction of Sn with O_2 at 800 °C and 1 mbar lead to the growth of SnO_2 NWs with average diameters of ≈50 nm and lengths up to ≈100 μm as shown in Fig. 1(a) which appeared as a uniform white layer on Si(0 0 1). The SnO_2 NWs grow by the vapour–liquid–solid (VLS) mechanism since we always find a nanoparticle at their ends as shown by the inset in Fig. 1(a) and the SnO_2 NWs do not grow on plain Si(0 0 1). We find that there is a statistical variation in the diameter of the SnO_2 NWs which depends on the size of the nanoparticles. The SnO_2 NWs exhibited clear peaks in the diffraction pattern corresponding to the tetragonal rutile crystal structure of SnO_2 in agreement with selected area electron diffraction (SAED) and high resolution transmission electron microscopy (HRTEM) analysis carried out previously on SnO_2 NWs verifying that they crystallize in the tetragonal rutile phase belonging to the P42/mnm space group with lattice constants of a = 0.4738 nm and c = 0.3186 nm [19].

We find that the exposure of SnO_2 NWs to H_2S leads to the formation of SnS_2 with a light-yellow color at 300 °C which turned progressively into yellow-brown at 400 °C. A typical SEM image of the SnS_2/SnO_2 NWs obtained at 300 °C is shown in Fig. 1(b) from which it is evident that the SnO_2 NWs maintain their integrity. Here it should be pointed out that the diameters of the SnO_2 NWs depicted in Fig. 1(a) are different to those in Fig. 1(b). The difference in diameters is attributed to the differences in the thickness of the catalyst layer and size of nanoparticles.

We observe a multitude of closely spaced diffracted peaks corresponding to the tetragonal rutile crystal structure of SnO_2 and hexagonal structure of SnS_2 after the exposure of the SnO_2 NWs to H_2S at 300 °C for 30 min and 60 min as shown in Fig. 2(a). Consequently there are two distinct phases but the exposure of the SnO_2 NWs to H_2S will result into the formation of SnS_2 at the surface of the SnO_2 NWs which has a definite impact on the electronic properties as described in detail below.

A typical EDX spectrum of the SnS_2/SnO_2 NWs obtained from SnO_2 NWs exposed to H_2S at 300 °C is shown as an inset in Fig. 3. The SnO_2/SnS_2 NWs consist of 40 at% Sn, 14 at% S and 38 at% O confirming the presence of S which is consistent with the observation of SnS_2 and SnO_2 in the GIXD spectra of Fig. 2(a) and (b). Here it should be noted that as-grown SnO_2 NWs are never perfectly stoichiometric and contain Sn and O vacancies which govern their electrical and optical properties. Furthermore, we observe the existence of SnO_2 and SnS_2 after the exposure of the SnO_2 NWs to H_2S at 400 °C for 30 min but the SnO_2 is fully converted into SnS_2 at 400 °C after 60 min as shown in Fig. 2(b). Temperatures above 500 °C lead to the elimination of the SnO_2 NWs and their conversion into hexagonal crystals of SnS_2 as shown by the inset in Fig. 1(b) and the diffraction pattern in Fig. 2(b). This is attributed to the rapid reduction of the SnO_2 NWs by the H_2 evolving from the decomposition of $H_2S \rightarrow H_2 + ½S$ which requires high temperatures in the range 750–1250 K.

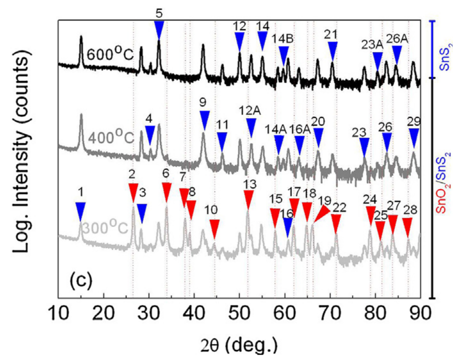

Fig. 2. GIXD diffraction pattern of SnO_2 NWs that were exposed to H_2S at 300 °C for 30 and 60 min. The diffracted peaks have been identified according to ICDD 01-071-5323 for SnO_2 and ICDD 00-023-0677 for SnS_2 and are labeled by red and blue arrows respectively in ascending order with increasing angle. In other words each arrow corresponds to a different angle and has a unique number and crystallographic plane associated with it as follows ▶ 1 (0 0 1), ▶ 2 (1 1 0), ▶ 3 (1 0 0), ▶ 4 (0 0 2), ▶ 5 (1 0 1), ▶ 6 (1 0 1), ▶ 7 (2 0 0), ▶ 8 (1 1 1), ▶ 9 (1 0 2), ▶ 10 (2 1 0), ▶ 11 (0 0 3), ▶ 12 (1 1 0), ▶ 13 (2 1 1), ▶ 14 (1 0 3), ▶ 15 (0 0 2), ▶ 16 (2 0 1), ▶ 17 (3 1 0), ▶ 18 (1 1 2), ▶ 19 (3 0 1), ▶ 20 (2 0 2), ▶ 21 (1 1 3), ▶ 22 (2 0 2), ▶ 23 (2 0 3), ▶ 24 (3 2 1), ▶ 25 (4 0 0), ▶ 26 (2 1 1), ▶ 27 (2 2 2), ▶ 28 (3 3 0), ▶ 29 (1 0 5). (b) GIXD diffraction pattern of SnO_2 NWs that were exposed to H_2S at 300, 400 and 600 °C for 60 min. ▶ 1 (0 0 1), ▶ 2 (1 1 0), ▶ 3 (1 0 0), ▶ 4 (0 0 2), ▶ 5 (1 0 1), ▶ 6 (1 0 1), ▶ 7 (2 0 0), ▶ 8 (1 1 1), ▶ 9 (1 0 2), ▶ 10 (2 1 0), ▶ 11 (0 0 3), ▶ 12 (1 1 0), ▶ 13 (2 1 1), ▶ 12A (1 1 1), ▶ 14 (1 0 3), ▶ 15 (0 0 2), ▶ 14A (2 0 0), ▶ 14B (1 1 2), ▶ 16 (2 0 1), ▶ 17 (3 1 0), ▶ 16A (0 0 4), ▶ 18 (1 1 2), ▶ 19 (3 0 1), ▶ 20 (2 0 2), ▶ 21 (1 1 3), ▶ 22 (2 0 2), ▶ 23 (2 0 3), ▶ 24 (3 2 1), ▶ 23A (2 1 0), ▶ 25 (4 0 0), ▶ 26 (2 1 1), ▶ 27 (2 2 2), ▶ 26A (1 1 4), ▶ 28 (3 3 0), ▶ 29 (1 0 5). (For interpretation of the references to color in this figure legend, the reader is referred to the web version of this article.)

The SnO_2/SnS_2 NWs obtained by exposing the SnO_2 NWs to H_2S at 300 °C for 30, 45 and 60 min exhibited broad PL with a maximum at ≈600 nm or 2.0 eV and are identical to the PL of the SnO_2 NWs exposed to H_2S at 300 °C for 60 min as shown in Fig. 3. Before elaborating further it should be noted that SnO_2 has a direct energy band gap of 3.7 eV but the even-parity symmetry of the conduction-band minimum and valence-band maximum states prohibits band-edge radiative transitions which has hindered the potential application of SnO_2 as an optoelectronic device. The broad PL at ≈600 nm or 2.0 eV is attributed to radiative recombination between defect states that are located energetically in the upper half of the energy band gap of the SnO_2 and hole states in the valence band as we have shown using ultrafast time resolved absorption transmission spectroscopy [20]. However the PL is also related to defects in the SnS_2 since it is an indirect band gap semiconductor known to exhibit

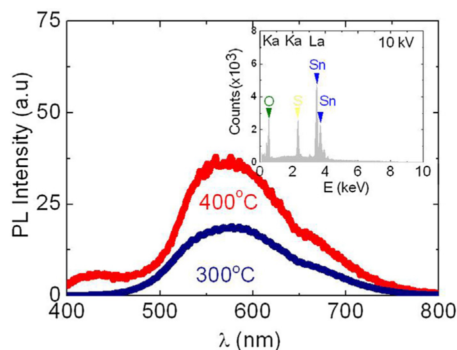

Fig. 3. PL spectra of SnO_2 NWs that were exposed to H_2S at 300 °C and 400 °C for 60 min obtained with an excitation of 260 nm at 300 K; inset shows a typical EDX spectrum of the SnO_2 NWs exposed to H_2S at 300 °C for 60 min.

defect emission at ≈2.0 eV. Interestingly the PL of the SnO_2 NWs exposed to H_2S at 400 °C for 60 min has two maxima, one at 580 nm or 2.14 eV due to radiative recombination via defects in the SnS_2 and a second peak at 420 nm i.e. 2.8 eV which according to Domingo et al. [21] is very likely to be related to a direct transition of SnS_2. The sulphur passivation of the SnO_2 NWs at 300 °C for 30, 45 and 60 min did not result in a dramatic change of the PL or the appearance of band edge emission from the SnO_2. However we observed an increase in the steady state absorption due to the formation of SnS_2 upon exposure of the SnO_2 NWs, grown on fused silica, to H_2S up to 875 nm i.e. 1.4 eV.

More importantly we find that the resistance of the SnO_2/SnS_2 NWs obtained after the exposure of SnO_2 NWs to H_2S at 300 °C for 60 min was smaller than that of the SnO_2 NWs. In particular the resistances of the SnO_2 NW assembly as-grown on 10 mm × 10 mm fused silica determined from four terminal measurements in accordance with O'Dwyer et al. [18] were 610, 560, 590 and 630 kΩ measured between the Ag contacts deposited at the four corners. In contrast the resistances of the SnS_2/SnO_2 NW assembly on 10 mm × 10 mm fused silica were three orders of magnitude smaller i.e. 510, 420 and 490 and 530 Ω. We have grown SnO_2 NWs on many different 10 mm × 10 mm fused silica substrates under identical growth conditions and have exposed these to H_2S at 300 °C for 60 min. The average resistance lies between 400 and 600 Ω which is significantly lower than the average resistance of the SnO_2 NWs that varied between 500 and 700 kΩ. Hence the exposure of the SnO_2 NWs to H_2S will result into the formation of SnS_2 at the surface of the SnO_2 NWs which has a definite impact on the electrical properties. In a way this is similar to what happens in SnO_2 NW sensors of H_2S. For instance it has been shown that the resistance of SnO_2 NWs drop by two orders of magnitude under 20 ppm of H_2S at 250 °C and is attributed to the modulation of the depletion layer and barrier height [22].

We observe a systematic difference between the resistance of the SnO_2 NWs which was three orders of magnitude higher than that of the SnS_2/SnO_2 NWs attributed to a higher one dimensional electron gas (1DEG) density and smaller barrier height at the surface which in turn depends on the energetic position of the Fermi level with respect to the conduction band (CB) edge at the surface. When the Fermi level E_F is close to the CB edge E_C at the surface, the depletion is small, and the carrier density in the core is larger. In contrast when the Fermi level resides energetically far below the CB edge the depletion region is larger and the carrier density in the core is smaller. In other words the Fermi level pinning at the surface governs the depletion and carrier density in SnO_2 NWs due to the large surface to volume ratio.

This may be understood further from the CB potential profile and 1DEG distribution of the SnO_2 and SnO_2/SnS_2 NWs shown in Fig. 4 which were determined from the self consistent solution of the Poisson–Schrödinger (SCPS) equations in cylindrical coordinates and the effective mass approximation. In such a calculation, Schrödinger's equation is solved in order to obtain the one dimensional sub-band energies and wave functions by taking into account a trial potential. Subsequently the 1DEG charge density is calculated by taking into account the thermal occupancy of each sub-band using Fermi–Dirac statistics and then solving Poisson's equation in order to determine a correction to the trial potential until the potential profile and charge distribution satisfy both Poisson and Schrödinger's equations. This has been described in detail elsewhere and its validity has been verified against analytical models [23]. The SCPS calculations have been carried out taking into account the effective mass and dielectric constants of SnO_2 and SnS_2, i.e. (a) $m^* = 0.2\,m_o$ and $\varepsilon_r = 13.5$ for SnO_2 [24–27], (b) $m^* = 1.646\,m_o$ and $\varepsilon_r = 10.3$ for SnS_2 [28], (c) $E_G = 3.7$ eV for SnO_2 and $E_G = 2.1$ eV for SnS_2, and (d) $\Delta E_C = 0.0235$ eV and $\Delta E_V = 1.5$ eV for the SnO_2/SnS_2 heterojunction [13]. We have also taken the Fermi

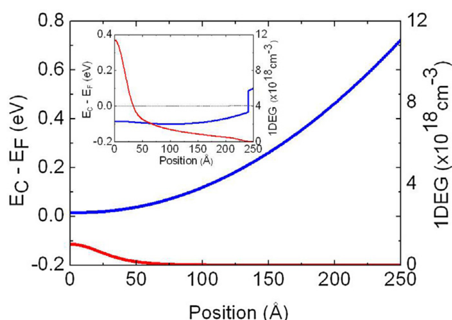

Fig. 4. Conduction band potential profile with respect to the Fermi level i.e. E_C–E_F shown in blue versus distance or position along the radius and 1DEG charge distribution for SnO_2 NWs; inset shows the potential profile and 1DEG charge distribution of an SnS_2/SnO_2 core–shell NW. (For interpretation of the references to color in this figure legend, the reader is referred to the web version of this article.)

level to be pinned ≈0.1 eV below the CB of SnS_2 [29], which is different to the case of SnO_2 NWs where the Fermi level is pinned ≈0.7 eV below the CB edge [30]. The CB edge potential energy E_C with respect to the Fermi level E_F taken at 0 eV i.e. $E_C(r)$–E_F versus distance or position along the radius is shown in Fig. 4 for a SnO_2 NW. To be more specific r = 0 nm corresponds to the core or center of the SnO_2 NW and the CB potential energy is shown with increasing distance or position along the radius, starting from the core and ending at the surface. The CB edge potential energy of the SnO_2 NW is shown on the left axis and the corresponding 1DEG charge distribution on the right axis of Fig. 4. The SCPS CB potential profile of the SnO_2 NW has a parabolic U-like shape and has a maximum 1DEG density of $\approx 1 \times 10^{18}$ cm^{-3} at the core or r = 0 nm. Similarly the SCPS CB potential profile of the SnO_2/SnS_2 NW has a parabolic U-like shape and a total of five sub-bands fall below the Fermi level in the core. The 1DEG has a maximum at the core and a volume density which is $\approx 1 \times 10^{19}$ cm^{-3} at the core or r = 0 nm that is an order of magnitude larger than that in the SnO_2 NWs and is one of the factors that may account for the smaller resistance of the SnS_2/SnO_2 NWs. The smaller resistance of the SnO_2/SnS_2 NWs cannot be associated with a higher mobility since the effective mass of electrons in SnS_2 is eight times larger than that in SnO_2 and the electron mobility in SnS_2 is ≈1 cm^2/Vs while that in the SnO_2 NWs is 70 ± 10 cm^2/Vs as determined previously from THz conductivity spectroscopy [31]. On the other hand it is possible that the smaller resistances of the SnS_2/SnO_2 NWs is due to a smaller barrier height at the surface of SnS_2 since the Fermi level is pinned ≈0.1 eV below the CB [29], which is different to the case of SnO_2 [30].

Interestingly we find that the complete conversion of the SnO_2 into SnS_2 NWs under H_2S at 400 °C resulted into even larger resistances than those of the SnO_2 NWs. More specifically we find that the average resistance of the SnS_2 NWs were of the order of several MΩ which may be related to the larger effective mass of electrons in SnS_2 and/or increased surface roughness since we observe the elimination of the SnO_2 NWs above 400 °C due to their reduction by the H_2 evolving from the decomposition of H_2S. It should be noted that the findings of this investigation is also relevant to those working on sensors not just photo catalysis or solar cells but further investigations into the surface chemical composition are required in order to understand better its effect on the electrical and optical properties of the SnO_2/SnS_2 NWs.

4. Conclusions

We have investigated the effect of sulphur passivation on the structural, electrical and optical properties of SnO_2 NWs but also the conversion of SnO_2 into SnS_2 NWs between 300 and 600 °C. We observe the existence of tetragonal rutile crystal structure of SnO_2 and hexagonal SnS_2 after the SnO_2 NWs have been exposed to H_2S at 300 °C for 30–60 min as confirmed by EDX analysis and high resolution GIXD. The SnS_2/SnO_2 NW assemblies exhibited broad PL at 2.4 eV and resistances between 400 and 600 Ω which are three orders of magnitude lower than the resistance of the SnO_2 NW assemblies that varied between 500 and 700 kΩ. This is attributed to a change of the Fermi level pinning at the surface of SnS_2 which results in smaller barrier heights and a larger one dimensional electron gas density in the core SnO_2. We find that the SnO_2 NWs are fully converted to hexagonal SnS_2 at 400 °C which resulted in the appearance of an additional PL peak at 2.8 eV but the SnS_2 NWs have considerably higher resistances of the order of MΩ. These findings are important for the exploitation of SnO_2/SnS_2 NWs in energy conversion and storage i.e. for the fabrication of solar cells but also for photo catalysis, super capacitors, batteries and sensors.

References

[1] E.C. Garnett, M.L. Brongersma, Y. Cui, M.D. McGehee, Annu. Rev. Mater. Res. 41 (2011) 269.
[2] D.B. Suyatin, C. Thelander, M. Bjork, I. Maximov, L. Samuelson, Nanotechnology 18 (2007) 105307.
[3] J.L. Hughes, S. Merchant, L. Fu, H. Tan, C. Jagadish, E.C. Camus, M. Johnston, Appl. Phys. Lett. 89 (2006) 232102.
[4] L. Vugt, S. Veen, E. Bakkers, A.L. Roest, D. Vanmaekelbergh, J. Am. Chem. Soc. 127 (2005) 12357.
[5] C. Gutsche, R. Niepelt, M. Gnauck, A. Lysov, W. Prost, C. Ronning, F.J. Tegude, Nano Lett. 12 (2012) 1453.
[6] N. Tajik, Z. Peng, P. Kuyanov, R.R. LaPierre, Nanotechnology 22 (2011) 225402.
[7] J. Lahiri, S. Senanayake, M. Batzill, Phys. Rev. B 78 (2008) 155414.
[8] J.Y. Hwang, S.Y. Park, J.H. Park, J.N. Kim, S. Koo, C. Ko, Thin Solid Films 520 (2012) 1832.
[9] J. Huh, M.K. Joo, D. Jang, J.H. Lee, G.T. Kim, J. Mater. Chem. 22 (2012) 24012.
[10] W.I. Park, J.S. Kim, G.C. Yi, M.H. Bae, H.J. Lee, Appl. Phys. Lett. 85 (2004) 5052.
[11] H. Tsukigase, Y. Suzuki, M.H. Berger, T. Sagawa, S. Yoshikawa, J. Nanosci. Nanotechnol. 11 (2011) 3215.
[12] T. Jiang, G.A. Ozin, A. Verman, R.L. Bedard, J. Mater. Chem. 8 (1998) 1649.
[13] Y.C. Zhang, Z.N. Du, K.W. Li, M. Zhang, D. Dionysiou, ACS Appl. Mater. Interfaces (2011) 1528.
[14] H. Chang, E. In, K.J. Kong, J.O. Lee, Y. Choi, B.H. Ryu, J. Phys. Chem. B 109 (2005) 30.
[15] T.S. Pan, D. De, J. Manongdo, A.M. Guloy, Y.L. Lin, H. Peng, Appl. Phys. Lett. 103 (2013) 093108.
[16] C.D. Lokhande, J. Phys. D: Appl. Phys. 23 (1990) 1703.
[17] Y.T. Lin, J.B. Shi, Y. Chen, C.J. Chen, P.F. Wu, Nanoscale Res. Lett. 4 (2009) 694.
[18] C. O'Dwyer, M. Szachowicz, G. Visimberga, V. Lavayen, S.B. Newcomb, C.M.S. Torres, Nat. Nanotechnol. 4 (2009) 239.
[19] M. Zervos, A. Othonos, D. Tsokkou, J. Kioseoglou, E. Pavlidou, Ph. Komninou, Phys. Status Solidi A 210 (2013) 226.
[20] A. Othonos, M. Zervos, D. Tsokkou, Nanoscale Res. Lett. 4 (2009) 828.
[21] G. Domingo, R.S. Itoga, C.R. Kannewurf, Phys. Rev. B 143 (1996) 536.
[22] A. Chowdhuri, P. Sharma, V. Gupta, K. Sreenivas, K.V. Rao, J. Appl. Phys. 92 (2002) 2172.
[23] M. Zervos, L.F. Feiner, J. Appl. Phys. 95 (2004) 1.
[24] H.J. van Daal, J. Appl. Phys. 39 (1968) 4467.
[25] M. Batzill, U. Diebold, Prog. Surf. Sci. 79 (2005) 47.
[26] K.J. Button, D.G. Fonstad, W. Dreybradt, Phys. Rev. B 4 (1971) 4539.
[27] Y. Mi, H. Odaka, S. Iwata, Jpn. J. Appl. Phys. 38 (1999) 3453.
[28] T.S. Pan, D. De, J. Manongdo, A.M. Guloy, V.G. Hadjiev, Appl. Phys. Lett. 103 (2013) 093108.
[29] D. Debtanu, J. Manongdo, S. See, V. Zhang, A. Guloy, Nanotechnology 24 (2013) 025202.
[30] A. Kar, Nanotechnology 22 (2011) 285709.
[31] D. Tsokkou, A. Othonos, M. Zervos, Appl. Phys. Lett. 100 (2012) 133101.